Near Wake Coherent Structures of a Turbulent Axisymmetric Wake

Taihang Zhu
Department of Aeronautics
Imperial College London
London SW7 2AZ, UK
taihang.zhu17@imperial.ac.uk

Georgios Rigas
Department of Aeronautics
Imperial College London
London SW7 2AZ, UK
g.rigas@imperial.ac.uk

Jonathan Morrison
Department of Aeronautics
Imperial College London
London SW7 2AZ, UK
j.morrison@imperial.ac.uk

ABSTRACT

The coherent structures of a turbulent axisymmetric bluff body wake are analysed using proper orthogonal decomposition (POD) and conditional POD based on synchronized near-wake velocity and base pressure measurements. The analysis confirms the persistence of the laminar unstable eigenmodes at high-Reynolds numbers (here $Re_D = 1.88 \times 10^5$). These correspond to a steady spatial-symmetry breaking mode and asymmetric unsteady vortex shedding modes in the near wake. Additionally, an unsteady axisymmetric bubble pumping mode representing the streamwise pulsation of the wake is found in the turbulent wake. The asymmetric modes are extracted in the wake of the axisymmetric body by performing conditional POD. The asymmetry of the wake, quantified using the centre of pressure (CoP), is correlated to the base pressure using conditional averaging. At the limits of the highly asymmetric wake or a perfectly symmetric wake, a high average pressure coefficient (low drag) is obtained. For the most probable state of the wake, a low-pressure coefficient (high drag) is obtained.

The above results provide insight on the coherent structures for canonical 3D bluff body geometries and guidance for drag reduction strategies.

EXPERIMENTAL SETUP

The experiment was conducted in the T2 wind tunnel in the Department of Aeronautics, Imperial College London. The test section is 1.15 m high, 1.61 m wide, and 4 m long, and equipped with a high-precision three-axis traverse. The inlet velocity is $U_\infty = 15$ m/s and the Reynolds number based on the diameter of the bluff body model ($D = 0.1965$ m) is $Re_D = 1.88 \times 10^5$. The turbulence intensity is less than 1% (10 kHz lowpass filtered) and the mean velocity variation on the cross-section of the wind tunnel is less than 1%. Figure 1 presents a schematic of the experimental setup and a 3D view of the model. A bullet-shaped axisymmetric body with a blunt trailing edge is located on the centre-line of the wind tunnel. The length-to-diameter ratio is $L/D = 6.48$, identical to the one studied in Oxlade *et al.* (2015) and Rigas *et al.* (2014). The model is carefully aligned with the inlet flow to achieve axisymmetric base pressure distribution after a long-time

average. Here, the mean pressure variation near the base edge is kept within 0.2 Pa. To measure the base pressure, 64 pressure tappings are distributed uniformly on the base (shown on the lower side of figure 1). They are connected to the Chell ESP-DTC pressure scanner to measure the pressure signal with 0.041 Pa resolution. A Pitot tube is mounted at (2D, -1.3D, 0) to measure the freestream velocity and the reference static pressure.
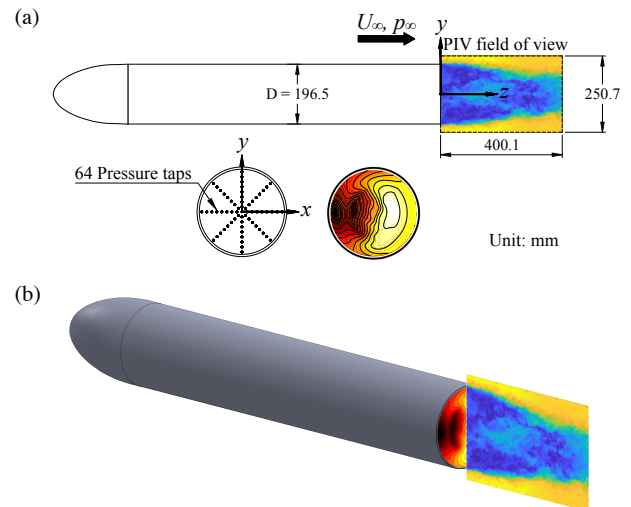

Figure 1. (a) A schematic of the experimental setup. The base pressure taps and the instantaneous base pressure distribution are shown on the lower side. (b) A 3D view of the model with the instantaneous PIV flow field and the synchronized base pressure measurement.

Time-resolved two-dimensional two-component PIV is used to measure the near wake velocity fields of the axisymmetric body. The field of view (FOV) and an example of the instantaneous velocity magnitude field are shown in figure 1(a). The FOV covers the near-wake area with a 400.08 mm x 250.68 mm rectangular plane pass through the body axis. A dual-port Litron LDY300 laser is used to provide a laser sheet for visualizing the seeding particles. A Phantom VEO 640L camera (with a resolution of 2560 x 1600 pixels), combined with a Nikkor 135 lens, is used to capture the FOV

images with a sampling frequency of 1440 Hz. LaVision DaVis 10 software is used to perform cross-correlation of the image pairs, producing the vector fields with a sampling frequency of 720 Hz. The velocity field is recorded on a 164 x 187 uniform grid, which gives a vector resolution of 2.53 mm. The velocity and pressure data are stored in 13 databases.

Each database consists of 5990 velocity snapshots separated by $\Delta U_\infty/D = 0.106$ (720 Hz sampling frequency). Each database is 8.32 s long giving a total sampling time of 108 s.
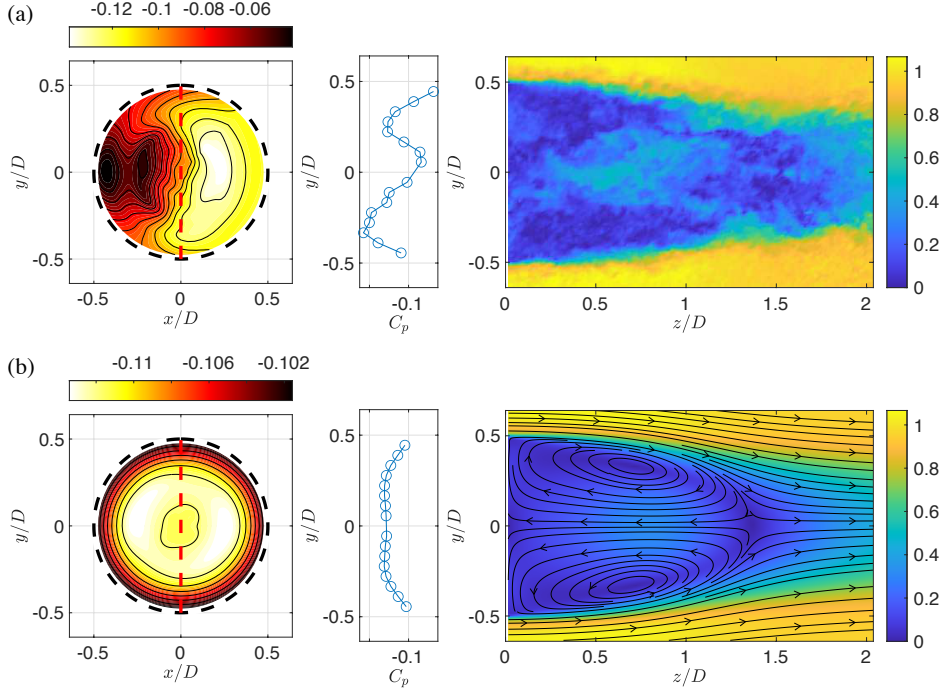
RESULTS

Figure 2. (a) The instantaneous and (b) the time-averaged PIV velocity field and the synchronized base pressure distribution. The left column shows the 2D base pressure distribution, with the black dashed line showing the base edge, and the red dashed line showing the PIV plane position. The middle column shows the base pressure at the PIV plane position. The right column shows the PIV velocity magnitude.
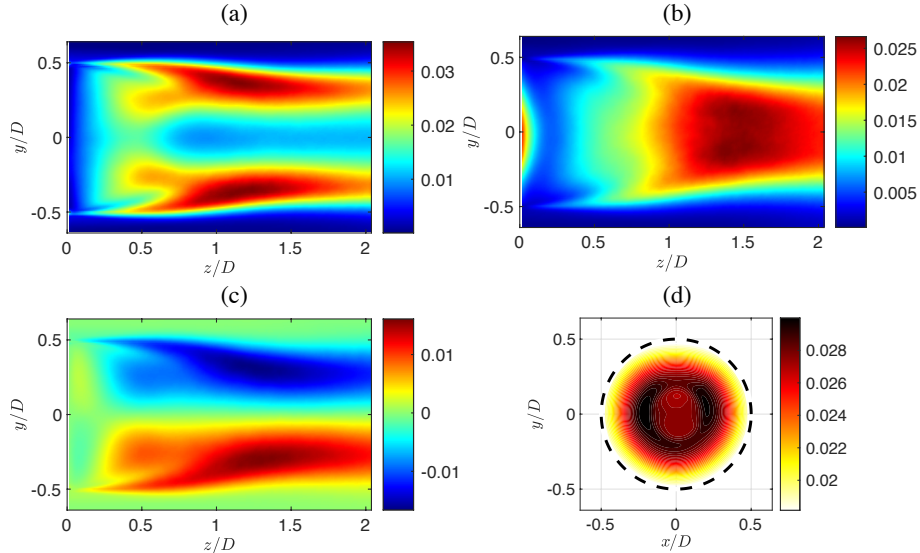

Figure 3. The second order properties of the wake: (a) Reynolds stress $\overline{u'_z u'_z}$; (b) Reynolds stress $\overline{u'_y u'_y}$; (c) Reynolds stress $\overline{u'_z u'_y}$; (d) the RMS value of the base pressure fluctuating component. (a), (b), and (c) shows the PIV plane, and (d) shows the base.

The observability of coherent structures is limited by the turbulent nature of high-Reynolds number wake. As is shown in figure 2(a), the turbulent wake is dominated by separation in the vicinity of the trailing edge. A turbulent shear layer is

formed due to the high velocity gradient between the inlet flow and the wake. The base pressure also fluctuates with the wake motion, in which a wide range of coherent structures is visible. A time-averaged velocity field and base pressure (figure 2b)

show that after time-averaging, both the velocity field and the base pressure distribution become symmetric. The second order properties of the wake (the Reynolds stress and the rms of the base pressure fluctuating component) are shown in figure 3. These are also symmetric. Therefore, the database is long enough to guarantee convergence, and the alignment of the body with the inlet flow is satisfactory.
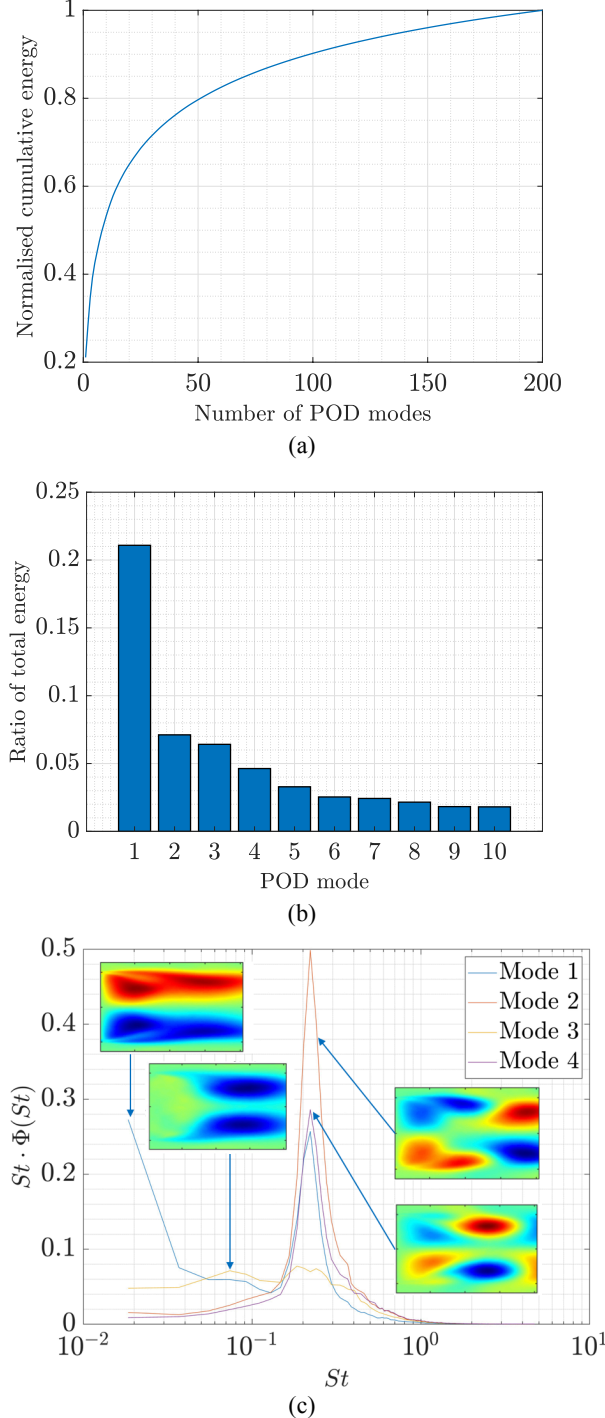

(a)

(b)

(c)

Figure 4. (a) The energy ratio and (b) normalized cumulative energy of each POD mode. (c) The pre-multiplied PSD spectrum of each POD mode amplitude and the main POD modes.

To extract coherent structures from the turbulent wake, POD is performed based on the horizontal and the vertical

velocity fields, after which the power spectral density (PSD) is used to analyse the time series of the mode amplitude (figure 4). The energy ratio and normalized cumulative energy of each POD mode are shown on figure 4 (a) and 4 (b), respectively. They show that the first POD mode takes up to 21% of the total energy, which is three times as high as the second POD mode (7%). The first four POD modes contribute about 40% of the total energy and represent the larger wake structures.

The premultiplied spectral density is used to analyse the time series of the mode amplitude (figure 4 c). There are multiple peaks near three distinct frequencies in the spectrum and show low-rank dynamics. The first peak is close to zero and the POD mode is of large scale, the shape resembling the unstable steady eigenmodes found in the laminar linear stability analysis (LSA) (Rigas et al. 2016). This mode is a steady spatial-symmetry-break mode with $St_D \sim 0$ and represents the stochastic switching of the wake between what appears to be a pair of quasi-steady states. A similar POD mode was also identified in a rectangular-sectioned bluff body by Fan et al. (2020) and Pavia et al. (2019) using time-resolved stereoscopic PIV. The peak close to $St_D = 0.06$ is the bubble-pumping mode. Mode 2 on the upper side has the same sign as that on the lower side, thus this mode is axisymmetric and represents the wake pulsation in the streamwise direction. Near the vortex shedding frequency ($St_D = 0.2$) there are three peaks, all of which are antisymmetric modes. The mode 2 and mode 4 are a pair of downstream travelling modes, representing the main coherent structures of the vortex shedding. These modes also resemble the unstable, unsteady modes found in the LSA. Since mode 1 represents the stochastic switching of the vortex shedding plane, there is some projection of mode 1 on the vortex shedding frequency.
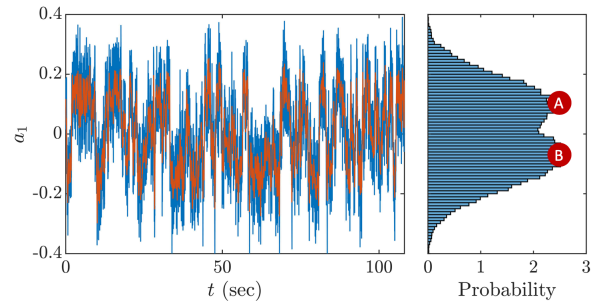

Figure 5. A time series of the first POD mode amplitude a_1. A PDF of a_1 is shown on the right-hand side, with A and B showing the quasi-stable positions.

The LSA result shows that the unstable mode triggering the transition from the steady wake to the unsteady one with vortex shedding is a spatial-symmetry-breaking mode (Rigas et al. 2016). In figure 3, however, the spatial symmetry is preserved when considering the absolute magnitude of each mode. Figure 5 shows a time series of first POD mode amplitude a_1. A PDF of a_1 is shown on the right-hand side, with A and B showing the quasi-stable positions. It shows that the mode amplitude is not stabilized near the centre. Instead, the mode amplitude is shifting between two states (A and B) resembling the bi-stability in the Ahmed body wake. It shows that the wake is asymmetric in the stable state and the spatial-symmetry shown in the POD modes (figure 3c) is a combination of two asymmetric states.
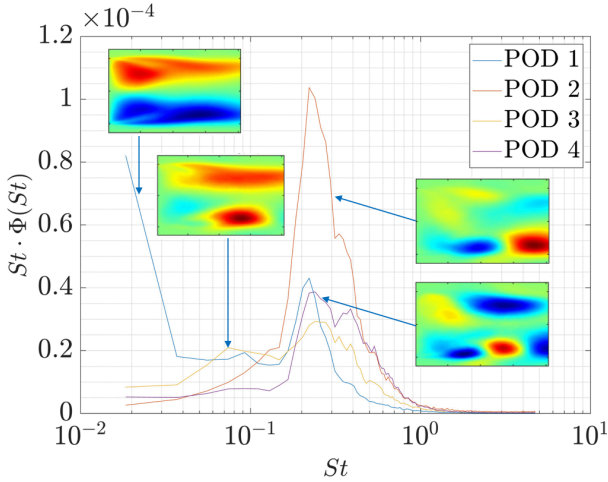
3

Figure 6. The conditional POD modes based on A position and the pre-multiplied PSD spectrum of each mode amplitude.

To extract the stable asymmetric POD modes, a conditional POD based on the velocity fields near one of the stable locations (A) is performed. Figure 6 shows the conditional POD modes and the corresponding PSD spectrum. It is clear that when the wake is in a stable state, all the POD modes lose symmetry. The most energetic mode near the vortex shedding frequency ($St_D = 0.2$) is biased toward the lower side and the upper side has largely disappeared, indicating the vortex shedding is asymmetric in nature. The bubble pumping mode ($St_D = 0.07$) is also asymmetric since the flow field is biased, whereas the upper side and the lower side of the mode retain the same sign, indicating the bubble pumping is the pulsation of the wake. The $St_D \sim 0$ mode is a quasi-steady, spatial symmetry-breaking mode and shows that the wake is asymmetric in the stable state. These results show that the turbulent wake in the stable state is spatial-symmetry breaking and consists of asymmetric POD modes.
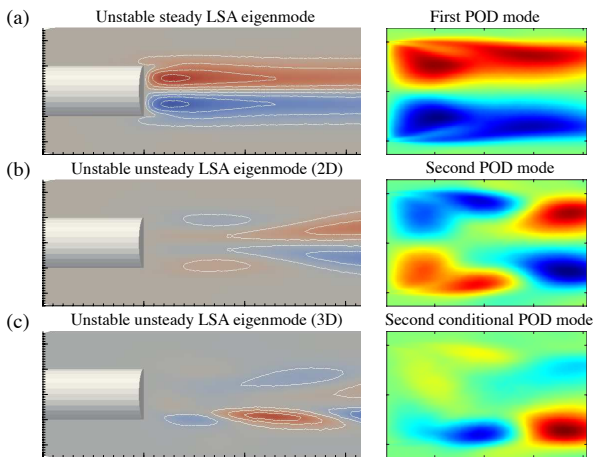

Figure 7. A direct comparison of the LSA eigenmodes (left column) with the POD and conditional POD modes (right column). (a) The first LSA mode (unstable steady mode) and the first POD mode; (b) the second LAS mode based on 2D axisymmetric base flow and the second POD mode; (c) the second LAS mode based on 3D asymmetric base flow and the second POD mode.

Here, we provide a direct comparison of the first two POD modes at $Re_D = 1.88 \times 10^5$ with the first two LSA

eigenmodes at $Re_D \sim 100$ to show that the laminar LSA modes persist in turbulent POD modes. Similar to the LSA, we will show that the conditional POD modes based on the flow field near the stable equilibrium is a more physical representation of the vortex shedding than the POD.

Figure 7(a) shows that the first unstable steady LSA eigenmode closely resembles the first POD mode. In the laminar wake, the first LSA mode breaks the 2D axisymmetric wake topology and transforms it into a 3D asymmetric steady wake (Rigas *et al.* 2016). Similarly, the first POD modes represent the stochastic switching of the wake in symmetry-breaking quasi-stable positions. Thus, the unstable steady laminar LSA mode persists in the high-Reynolds number wake and they represent the same symmetry-breaking phenomenon.

The main structures of the second LSA mode, which transforms the steady base flow into the unsteady wake, is also found in the second POD mode in both 2D and 3D wake (figure 7b and c). The LSA and POD modes shown in figure 6(b) are based on the 2D symmetric base flow. Rigas *et al.* (2016) shows that this LSA eigenmode is not an accurate representation of the second bifurcation and leads to an incorrect prediction of the bifurcation threshold, since the stability of the 2D base flow is broken by the first bifurcation. Similarly, the POD mode based on the 2D flow is not an accurate representation of the vortex shedding phenomenon, since the 2D flow is not stable. The true LSA eigenmode for the second bifurcation is calculated with the 3D base flow and accurately predicts the Hopf bifurcation (Rigas *et al.* 2016). A similar POD mode is found in the turbulent wake by the conditional POD based on the flow near the stable equilibrium (figure 6c). Compared to the symmetric POD mode (figure 6b), the symmetry-breaking POD mode is based on flow near stable equilibrium and closely resembles the true LSA mode, thus representing a more physical vortex shedding phenomenon.
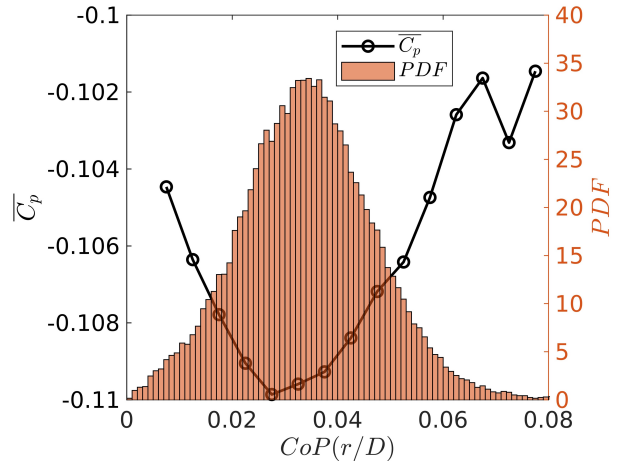

Figure 8. The relationship between the base pressure coefficient and the CoP.

The symmetry of the wake is quantified based on the centre of pressure (CoP) and correlated to the base pressure (and thus drag) using conditional averaging. As is shown in figure 8, near the large probability (around $r/D = 0.03$), the base pressure is low, indicating that for the most probable state of the wake, low base pressure and high drag are obtained. Since the concentration of the CoP represents the multi-stability nature of the wake, breaking the multi-stability is a

promising way of increasing base pressure and reducing drag. Away from $r/D = 0.03$, the base pressure increases toward the base centre and the base edge, showing that both the

symmetric wake and the highly-asymmetric wake possess higher base pressure and lower drag.
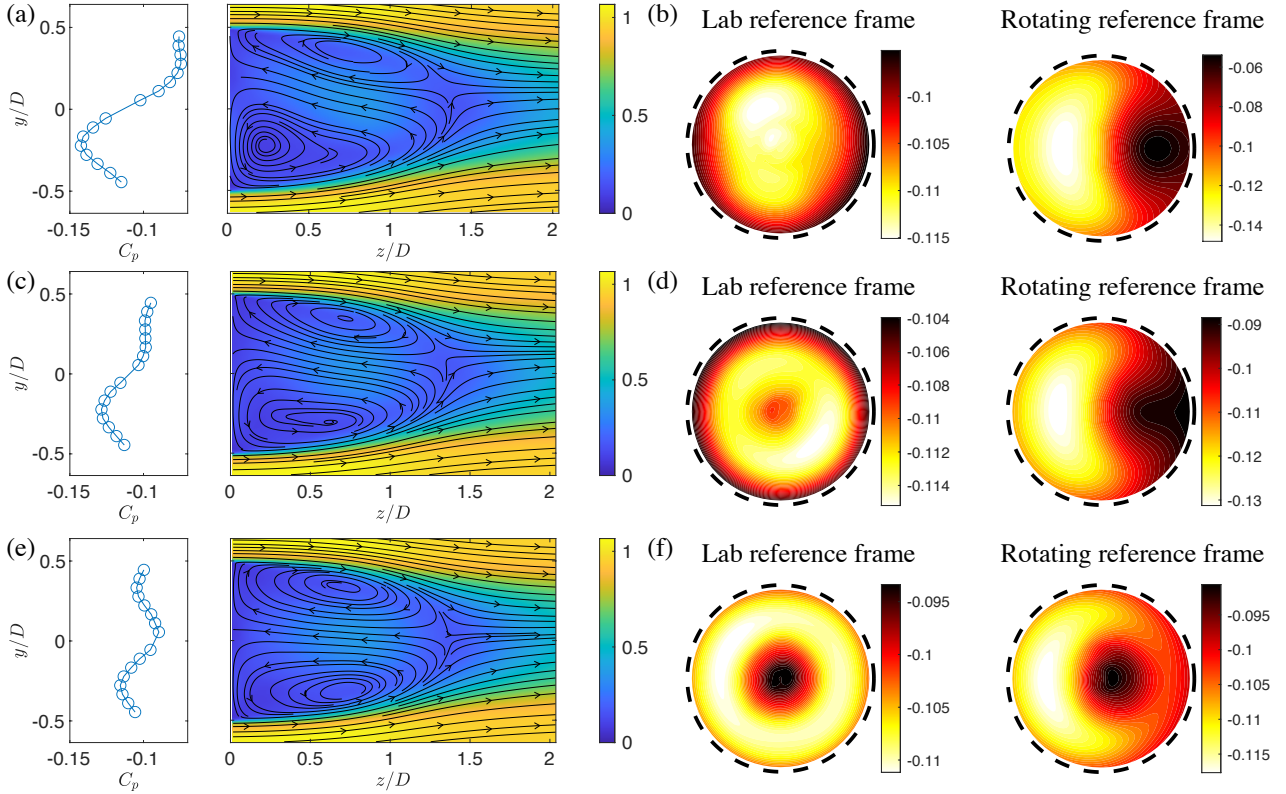

Figure 9. Conditional averaged flow fields, base pressure, and base pressure in a rotating frame of reference for (a, b) CoP > 0.05, (c, d) 0.023 < CoP < 0.027, and (e, f) CoP < 0.015.

Further insight into the relationship between the symmetry of the wake and the base pressure is provided by conditionally selecting the PIV snapshots and the synchronized base pressure according to the CoP. Figure 9 shows conditional averaged flow fields, base pressure, and base pressure in a rotating frame of reference for CoP > 0.05, 0.023 < CoP < 0.027, and CoP < 0.015. The synchronized PIV and base pressure shown on figure 9 (a) (c) and (e) are further filtered with $CoP_{1D} > 0$, where CoP_{1D} is the 1D base pressure measured simultaneously with the PIV flow fields. Following Rigas et al. (2014) and Grandemange et al. (2013), the base pressure in a rotating reference frame is achieved by rotating the base pressure according to the azimuthal component of the CoP (CoP_{θ}). The instantaneous base pressure fields are rotated to move CoP_{θ} to zero, after which they are averaged to get the base pressure in a rotating reference frame.

Figure 9(a, c, e) shows two asymmetric circulation bubbles in the near wake with a low-pressure region near the larger one. In the vicinity of the stagnation point on the base, there is a high-pressure region that shifts with the level of wake asymmetry. In the highly-asymmetric wake (figure 9a), the stagnation point on the base and the high-pressure region are close to the edge. The large circulation bubble on the other side leads to a low base pressure region, especially near the bubble centre. As the CoP decreases, the high-pressure region near the stagnation point on the base drops, while the base pressure rise near the large circulation bubble does not compensate for the base pressure drop (figure 9c). Thus, the overall base pressure drops and leads to a low-pressure, high-

drag case near 0.023 < CoP < 0.027. As the wake becomes more symmetric (figure 9f), both the base pressure near the stagnation point and the base pressure near the large circulation bubble rises, which leads to a high-pressure, low-drag case. Thus, the transition of the base pressure with the CoP is the combined effect of the low-pressure zone near the circulation bubbles and the high-pressure zone near the stagnation point on the base.

A two-dimensional base pressure distribution in the laboratory reference frame and in the rotating reference frame is shown on figure 9(b, d, f). Like figure 9(a), in the rotating reference frame, there exists a high-pressure zone near close to the stagnation point location on the base. As the CoP decreases, the base pressure in a rotating reference frame becomes more symmetric, with the high-pressure region gradually moving from the base edge towards the centre.

CONCLUSIONS

The turbulent axisymmetric bluff body wake ($Re_D = 1.88 \times 10^5$) is analysed using POD, conditional POD, and conditional average, based on the synchronized PIV and base pressure measurement of the near wake velocity field on a plane parallel to the streamwise direction.

The POD modes uncover three kinds of motion in the wake. The first POD mode is a steady symmetry-breaking mode ($St_D \sim 0$) representing the stochastic switching of the vortex shedding plane in the azimuthal direction. The second and fourth POD modes, coupled with the first POD mode, represent the unsteady vortex shedding ($St_D = 0.2$). An

axisymmetric POD mode is found near the bubble pumping frequency ($St_D = 0.07$), which represents the global streamwise pulsation of the wake. By performing conditional POD with the flow field near the stable equilibrium, the asymmetric modes are extracted from the near wake of axisymmetric body.

A direct comparison of the laminar LSA modes with the turbulent POD modes shows that the unstable laminar modes persist in the turbulent wake. The first LSA eigenmode corresponds to the first POD mode, both of which represent the steady spatial-symmetry breaking phenomenon in the wake. The second LSA eigenmode based on the unstable 2D base flow and the 3D stable base flow can be found in the second POD mode based on the unstable symmetric flow and the stable asymmetric flow. The conditional POD mode based on the flow near the stable equilibrium is a more physical representation of vortex shedding.

The symmetry of the wake is quantified based on the CoP and correlated with the base pressure (and thus drag) using conditional averaging. For the most probable state of the wake, a low-pressure coefficient is obtained (high drag). At the limits of the highly asymmetric wake or a perfectly symmetric wake, a high average pressure coefficient (low drag) is obtained. The transition of the base pressure with the CoP is the combined effect of the low-pressure zone near the circulation bubble and the high-pressure zone near the stagnation point on the base.

The above results provide insight to the coherent structures for canonical 3D bluff body geometries and help to guide the development of drag reduction strategies.

REFERENCE

Fan, Yajun, Xia, Chao, Chu, Shijun, Yang, Zhigang & Cadot, Olivier 2020 Experimental and numerical analysis of the bi-stable turbulent wake of a rectangular flat-backed bluff body. Physics of Fluids 32, 105111.

Grandemange, Mathieu, Gohlke, Marc & Cadot, Olivier 2013b Turbulent wake past a three-dimensional blunt body. part 1. global modes and bi-stability. Journal of Fluid Mechanics 722, 51–84.

Oxlade, A. R., Morrison, J. F., Qubain, A. & Rigas, G. 2015 High-frequency forcing of a turbulent axisymmetric wake. Journal of Fluid Mechanics 770, 305–318.

Pavia, Giancarlo, Varney, Max, Passmore, Martin & Almond, Mathew 2019 Three dimensional structure of the unsteady wake of an axisymmetric body. Physics of Fluids 31 (2), 025113.

Rigas, G., Oxlade, A. R., Morgans, A. S. & Morrison, J. F. 2014 Low-dimensional dynamics of a turbulent axisymmetric wake. Journal of Fluid Mechanics, 755 R5.

Rigas, G., Esclapez, L. & Magri, L. 2016 Symmetry breaking in 3D wakes. In Proceedings of the Summer Program. Center for Turbulence Research, Stanford University, arXiv:1703.07405.